Non-local Chemical Potential Modulation in Topological Insulators Enabled by Highly Mobile Trapped Charges

Yasen Hou[1], Rui Xiao[1], Senlei Li[1], Lang Wang[1], Dong Yu[1*]

[1]Department of Physics, University of California, Davis, California 95616, USA

*Corresponding author. Email: yu@physics.ucdavis.edu

ABSTRACT

Topological insulators (TIs) host unusual surface states with Dirac dispersion and helical spin texture and hold high potential for applications in spintronics and quantum computing. However, unintentional doping due to native defects in these materials creates a key obstacle to displaying their desired unique spin and charge transport properties. Here, we report a simple and effective method that can in-situ tune the chemical potential in $Bi_{2-x}Sb_xSe_3$ nanoribbon devices, with a magnitude significantly larger than traditional electrostatic gating. An electric field parallel to a device channel alters the chemical potential both in channel and out of channel. We demonstrate that such modulation is enabled by fast charge diffusion among defect states, further visualized by photocurrent mapping. Our observations enable dynamic chemical potential engineering, providing tremendous opportunities for investigating fundamental transport mechanisms of charge and composite particles, such as excitons, in TIs.

KEYWORDS: chemical potential modulation, topological insulators, charge traps, scanning

photocurrent microscopy, exciton condensation

INTRODUCTION

Manipulating chemical potentials of materials by defect engineering plays a crucial role in semiconductor electronics and is specifically important in TIs because unintentional doping in these materials creates a key obstacle to displaying their desired unique spin and charge transport properties. Control of the chemical potential in these materials is challenging but crucial to realizing the hotly pursued exotic physics, including efficient spin generation,[1-2] Majorana Fermions,[3-4] and exciton condensation.[5-6] Chemical doping,[7-8] molecule adsorption,[9] electron or alpha particle irradiation,[10-11] potassium deposition,[12] and controlled structural deformation[13] have all been employed to bring the chemical potential into the TI's bulk bandgap. Nevertheless, for both fundamental studies and electronic applications, a dynamical method of adjusting the chemical potential during device operation is desired, but by far is largely limited to electrostatic gating.[14-15] Back gating is known to be efficient only at influencing the carrier concentration at the TI bottom surface,[16] while the fabrication of top gates involves sophisticated processes and tends to degrade the material properties.[17-18] Recently photo-gating has also been demonstrated in $(Bi,Sb)_2Te_3$ devices, but it requires interfacing an optically thin TI layer with specific substrates such as $SrTiO_3$.[19-20]

Charge traps can significantly affect electronic properties, as manifested in nonvolatile memory[21-22] and persistent photoconductivity.[23-24] TIs are vulnerable to various kinds of defects, especially when placed in ambient environments.[17, 25] While these defect states are previously largely viewed as unintended electron donors detrimental to applications, they can be actively manipulated to engineer the TI electronic properties. Fundamentally, the effects of

defects on TI surface charge transport are nontrivial. In the presence of point defects, the TI surface states are predicted to be inherently against localization.[26-29] These theoretical predictions require further experimental inputs.

Here we show that the active manipulation of the trapped charges offers a powerful way to control the chemical potential. Using photocurrent imaging, we visualized the diffusion of trapped charges by over hundreds of micrometers within minutes, at room temperature in $Bi_{2-x}Sb_xSe_3$ nanoribbons. Compared to previous methods, our approach neither introduces external defects as in chemical doping, nor requires creating a foreign interface as in electrostatic or photo-gating. Cooling the devices under longitudinal electric field results in intrinsic TIs, which demonstrate ambipolar conduction and reveal very long photocurrent decay length, indicating non-trivial transport of photogenerated charge carriers.

EXPERIMENTAL SECTION

Single-crystal $Bi_{2-x}Sb_xSe_3$ nanoribbons (x ranging from 0.15 to 0.4) were grown by a chemical vapor deposition (CVD)[5, 30] method in a Lindberg Blue M tube furnace. Bi_2Se_3 powder (99.999%, Alfa Aesar) mixed with Sb powder (99.999%, Alfa Aesar) was placed at the centre of the tube furnace. Se pellets (99.999%, Johnson Matthey Inc.) were placed upstream at 16 cm. A silicon substrate coated with a 10 nm Au film was placed downstream 14 cm from the centre of the furnace. Argon gas was used to transfer vapour from the source materials to the growth substrate at a 150 sccm (standard cubic centimetres per minute) flow rate. During the 5 hours of growth time, the temperature at the centre of the furnace was maintained at 680 °C and the pressure was maintained at room pressure. The furnace was then cooled down to room

temperature over approximately 3 hours. The as-grown nanoribbons were transferred to Si substrates covered by 300 nm SiO_2, where single nanoribbon field effect transistor (FET) devices were fabricated following the standard electron beam lithography process. Top metal contacts (10 nm Ti / 290 nm Au) were made using an electron beam evaporator (CHA). A typical device is shown in Figure 1b.

All measurements were carried out in a cryostat (Janis ST-500) under 10^{-7} Torr. Current-voltage curves were measured through a current preamplifier (DL Instruments, model 1211) and a NI data acquisition system. Scanning photocurrent microscopy (SPCM) measurements were performed using a home-built setup based upon an Olympus microscope. A 532 nm CW laser was focused by a 10× NA = 0.3 objective lens to an approximately 3-μm spot and raster scanned on a planar nanoribbon device by a pair of mirrors mounted on galvanometers. Both reflectance and photocurrent were simultaneously recorded to produce a 2D maps. The laser power was controlled by a set of neutral density (ND) filters and was measured by a power meter underneath the objective lens.

RESULTS AND DICUSSION

Non-local conductance modulation in $Bi_{2-x}Sb_xSe_3$ nanoribbons

After a longitudinal electric field was maintained in a channel of the device shown in Figure 1b for a few minutes, the channel conductance gradually changed by a few percent (Figure S1). More surprisingly, the electric field not only changed the conductance in the channel where it was applied, but also outside that channel. In device #1, the conductance in

channel CD (G_{CD}) increased by 11% in hundreds of seconds at 300 K, when V_{AB} = 1 V was applied in channel AB 232 μm away (Figure 1c). After V_{AB} was removed, G_{CD} decreased to the initial value in a similar time. Reducing V_{AB} results in a smaller change in G_{CD} and the reversing of the electric field direction led to the opposite change in conductance. Though the conductance change was highly reproducible in all tested $Bi_{2-x}Sb_xSe_3$ nanoribbon devices, pure Bi_2Se_3 nanoribbon devices did not show such a behavior likely caused by their high conductivity.

Field cooling effects and persistent chemical potential shift at low temperatures

The change rate of the non-local conductance sensitively depended on temperature. At 175 K, the response took more than 10^4 s (Figure 1d). After cooling the device under a fixed bias from room temperature to 77 K, the conductance change was maintained indefinitely even after the applied electric field was removed. Furthermore, at low temperature the conductance could no longer be modulated by a longitudinal electric field. Nevertheless, conductance was recovered to the original level if the device was warmed to room temperature. Several cooling/warming cycles were then performed on device #2 with different biasing conditions during cooling (Figure 2). Gate responses confirmed that the conductivity change originated from the chemical potential (or Fermi level, E_F) shift. The *n*-type device exhibited strong gate dependence (Figure 2e, h) when cooling with all contacts floating. Channel AB appeared to be more *n*-type than CD, presumably because of slight spatial doping variation during the sample growth. G_{CD} reached a minimum at V_g = - 75 V, indicating that E_F was tuned across the Dirac point by V_g. However, after cooling with V_{DB} =

5 V, G_{AB} increased more than 10 times and completely lost gate response, while the minimum point in G_{CD} in the gate scan shifted close to V_g = 0 V (Figure 2d, g). Cooling with V_{AB} = 1 V shifted E_F in opposite directions (Figure 2f, i) and made channel AB ambipolar. The electric field can thus either raise or lower E_F depending on the field direction and the location. E_F rises beyond the low potential contact, and falls in the channel and beyond the high potential contact. These observations are highly repeatable in more than 10 devices measured to date.

The field-controlled bi-directional E_F shift enables the design of biasing conditions to engineer spatial distributions of E_F, for instance, to create n^+-n and p-n junctions in TIs. Furthermore, the chemical potential manipulation achieved with the longitudinal field is significantly more effective than conventional electrostatic gating. The conductivity can be tuned by more than 10 times via field cooling (Figure 2d), while sweeping V_g over a range of 250 V across the 300 nm oxide only leads to a maximum 25% conductivity change. This larger tunability is likely caused by two reasons. First, E_F at both top and bottom surfaces can be adjusted by longitudinal field, while the back-gate mainly affects the bottom surface. Second, the trapped charges are much closer to the surface states, providing more effective E_F control.

Visualizing fast diffusion of trapped charges by photocurrent imaging

To gain further insights in the mechanism of the non-local conductance change, we employ SPCM, where photocurrent is measured as a focused laser is raster scanned over the device plane to form a 2D map. Photocurrent is generated if the locally injected electrons and holes are separated in the presence of an electric field. As a result, this method provides

information about the local electric field distribution originated from doping gradient.[31] Device #1 was first cooled, with all contacts floating, to 200 K. A photocurrent image showed random photocurrent spots with small magnitude (Figure 3a), which had been reported before and were attributed to the random fluctuation of chemical potential in TIs.[32-33] Photocurrent was also observed when the laser was on the electrodes, which we attributed to thermoelectric effects.[5] Then V_{CB} = 4 V was held for 3 hrs to create large doping gradient. After V_{CB} was reduced to zero at t = 0 s, SPCM images were taken consecutively to examine the evolution of the electric field distribution. At t = 10 s, a strong negative photocurrent peak appeared close to contact B (Figure 3a). Over time, this peak moved towards contact C and gradually became broader and weaker. After 12000 s, the photocurrent image had recovered to that before the bias was applied. V_{CB} = - 4 V yielded similar results, with both the polarity and the shift direction of the photocurrent peak reversed (Figure 3b). The peak position follows well with the square root of time (Figure 3c), as expected from a diffusion process.[31] The fitting yields a diffusion constant of 2.3 × 10^{-7} cm^2/s at 200 K. Similar SPCM measurements performed at 300 K showed the same trend with the recovery process taking less than 180 s (Figure S2).

These visualized evolving chemical potential distributions provide strong evidence for the diffusion of certain trapped charges at the TI surface. These localized charges do not directly contribute to electrical conduction but provide local electrostatic gating and enable E_F shift. Potential origins for the trapped charges are electrons/holes trapped at defect states, ions such as Au and selenium, and surface adsorbed molecules such as water and oxygen. The trapped charges traveled by over 200 μm within 180 seconds at room temperature and

were not blocked by metal contacts.[31] Thus ion diffusion and molecule diffusion are highly unlikely, as they usually migrate much slower in solids.[34-36] The devices are placed in high vacuum and the bottom surfaces of the devices can also be affected (Figure 2), further excluding the possibility of surface adsorbed molecule diffusion. Au migration from the contacts onto the TI surface[37-38] does not explain the observations, since TI devices fabricated with Au-free contacts exhibited similar non-local E_F shift effects (Figure S3). In addition, spatially resolved energy dispersive X-ray spectroscopy (EDS) did not show any indication of ion (Se, Sb and Bi) migration after biasing (Figure S4).

We attribute the observations to field-driven migration of electrons (or holes) trapped at defect states. In contrast to ions and molecules, the hole hopping among traps is not affected by metal contacts, in agreement with our experimental results. Our observation that photoexcitation at 77 K led to persistent conductance increase (Figure S5) provides further evidence: though the migration of trapped holes is suppressed at this temperature, photoexcited hot charge carriers can be captured/de-captured by the traps and lead to local E_F modulation.[23-24] This photo-assisted trapping/de-trapping is amenable to designing and controlling chemical potential distributions via optical writing at low temperature. By exposing an area of the device to a high-power laser, n-n^+ junctions are created at the edges of the writing area, as visualized by SPCM (Figure S6).

Numerical simulation of the diffusion and drift of trapped charges

Photocurrent mapping shows that trapped charges build up at the low potential contact (Figure 3a, b), indicating the trapped charges are positively charged, i.e., holes. To more

quantitatively understand this process, we consider a 1D model describing diffusion-drift along the nanoribbon axis, where the trapped hole density $n(x,t)$ follows the continuity equation

$$\frac{dn}{dt} = \mu E \frac{dn}{dx} - D \frac{d^2n}{dx^2} \quad (1)$$

Here, n is the concentration of localized charges, E is the electric field, μ is their mobility, and D is their diffusion coefficient (Einstein relation $D = \mu k_B T/q$ is assumed). Because of a small contact resistance (< 8% of the channel resistance), the electric field is small outside the channel but not exactly zero. The partial differential equation is solved by finite element method with a mesh size of 1 μm. The time step used in the simulation is 0.2 ms above 200K and 2.5 ms below. Charge continuity and current continuity are applied at all boundaries. A uniform trapped hole density is assumed as the initial condition n (t = 0) = n_0. Temporal evolutions of n under $V_{AB} = \pm 0.5\ V$ are presented in Figure S7.

The simulated n at the center of probing channel CD follows well with the measured conductance change (Figure 1d) at all temperatures. We notice that as G_{CD} is close to saturation, its evolution is slightly slower than predicted by the diffusion model (Figure 1d) likely because of the repulsive interaction between the trapped charges which is not considered in the model and tends to reduce the diffusion rate.[39] The simulation also agrees with the bias dependence as in Figure 1c (Figure S7). D extracted from the model is 2.1 × 10^{-6} cm^2/s at 300 K, corresponding to a mobility of 8.0 × 10^{-5} cm^2/Vs. D is temperature sensitive and follows well an Arrhenius behavior with an activation energy of 0.179 eV (Figure 1e). The D value extracted at 200 K is 2.6 × 10^{-7} cm^2/s and agrees well with that extracted from the photocurrent peak shift (Figure 3c).

Control over the photogenerated carrier propagation distance

The large E_F tunability achieved by the longitudinal electric field provides a practical and efficient way to suppress bulk conduction and reveal the non-trivial surface charge transport of the TI materials. For example, we have recently demonstrated millimeter-long transport of photoexcited carriers up to 40 K in $Bi_{2-x}Sb_xSe_3$ nanoribbons,[5] which provided key experimental evidence for theoretically predicted topological exciton condensate.[6, 40] Such efficient transport of photocarriers is only observed when E_F is close to the Dirac point and at low temperatures. Here by cooling with different biasing conditions, we can selectively control the photocarrier transport distance in different channels and turn on or off the exotic effect at will. We first started with a device (device #1) with E_F too high above the Dirac point to exhibit the non-local photocurrent. When cooled to 77 K with all contacts floating, the device only showed localized and weak photocurrent near the contacts, originating from photo-thermoelectric effects (Figure 4a).[5] However, after cooling with V_{BC} = 4 V, photocurrent was much stronger and extended far beyond the contacts, in the region to the right of contact C (Figure 4b). This is consistent with E_F lowering in this region. Photocurrent images taken with different connection configurations are all in perfect agreement with the expected E_F distribution as shown in the bottom diagram of Figure 4b. Similarly, when cooled with V_{DC} = 0.1 V, long photocurrent decay was observed to the left of contact C as expected (Figure 4c). V_g alone cannot turn on the photocurrent without the use of longitudinal electric field.

The electric field can also be used to turn off the photocurrent in the desired channel of

the device. This time we started with a different device (device #3), in which E_F was initially close to the Dirac point as confirmed by gate scans (Figure S8). Extended photocurrent signal was observed on the entire device when cooling with all contacts floating (Figure 4d). Fitting of the photocurrent cross sections shows a photocurrent decay length (L_d) up to 260 μm at 77 K (Figure S9). Cooling with V_{CE} = - 4 V increased E_F to the right of contact C and led to vanishing photocurrent in this region (Figure 4e). Cooling with V_{CE} = 4V led to vanishing photocurrent to the left of contact E (Figure 4f). The field effects therefore can be used to engineer the E_F distribution in a TI device, toward potentially controlling the critical temperature of exciton condensation and the coherence length of excitons in selected regions.

Discussion on charge localization in TIs

All our experimental observations are consistent with thermally activated charge hopping among localized defect states.[41-46] Nevertheless, it has been established that defect states at TI surfaces are inherently against localization.[26-29] Consequently, the defects that account for these charge traps are more likely in the bulk instead of at the surface. Band bending at the TI surface[8, 47] presumably provides an energy barrier, resulting in long lived trapped charges in the TI bulk. The charges trapped at these localized states act as local gating and influence E_F at the TI surface through electrostatic coupling. Typical defect density in Bi_2Se_3 is in the order of 10^{19} cm^{-3}.[29, 48-49] From the gate scans in Figure 2 and using a parallel-plate capacitor model, we estimated trapped charge density in our single-crystal $Bi_{2-x}Sb_xSe_3$ nanoribbons on the order of 10^{18} cm^{-3}, a lower limit of the trap site density. This corresponds to a separation of 5-10 nm between neighboring trap sites, which is expected to allow direct charge

hopping.[45-46] Another interesting possibility is surface-state-mediated charge hopping among bulk defects. In this scenario, delocalized surface states serve as a bridge, facilitating charge hopping even when the separation between defects is large. Further work is necessary to clarify on the hopping mechanism among trap states in TIs. We note that only $Bi_{2-x}Sb_xSe_3$ nanoribbons with $x < 0.4$ were studied due to the limitation of our growth method. It has been demonstrated that $Bi_{2-x}Sb_xSe_3$ nanoribbons remain a TI up to $x = 1.5$.[50] Thus, we expect that the long L_d and the non-local E_F modulation can still be observed up to this doping range.

CONCLUSION

In summary, we demonstrate a practical approach that can tune the chemical potential across the Dirac point of the TI surface states at both top and bottom surfaces, without the requirement of complex device fabrication. Our approach can shift E_F in a significantly wider range than traditional electrostatic gating. An electric field parallel to the device channel drives the migration of trapped holes at the TI surface, lowering (raising) E_F on the low (high) potential side. The trapped holes accumulated at the contacts can diffuse out of the channel, leading to non-local E_F modulation up to hundreds of micrometers away. Our method can be used to create *p*-*n* or *n*-n^+ junctions, by engineering the applied electric field or by optical writing. As visualized by photocurrent mapping, the trapped holes diffuse with a diffusion coefficient of 2.1×10^{-6} cm^2/s at room temperature and an activation energy of 0.179 eV. Bulk-insulating TIs can be achieved by field-cooling, revealing the exotic properties of the topologically nontrivial surface states. For instance, photogenerated charge carriers were shown to propagate over 100 μm at 77 K in field-cooled devices, demonstrating the potential control of exciton condensates. The developed experimental method may also be applied to

control chemical potentials and to investigate trapped charge diffusion in a broad range of materials.

ASSOCIATED CONTENT

SUPPORTING INFORMATION

The Supporting Information is available free of charge at (to be filled).

In-channel conductance change under electric field, visualization of field-induced doping gradient by SPCM at 300 K, control experiment with Au-free electrodes, energy dispersive X-ray spectroscopy (EDS) data before and after applying electric field, photo-induced persistent conductance change at 77 K, optically induced E_F shift, numerical modeling of electric-field-driven trapped charge migration, field cooling effects on gate responses for device #3, and field effects on photocurrent distribution at 77 K.

AUTHOR INFORMTION

Corresponding Author

Dong Yu - Department of Physics, University of California, Davis, California 95616, USA. Email: yu@physics.ucdavis.edu

Authors

Yasen Hou – Department of Physics, University of California, Davis, California 95616, USA.

Rui Xiao – Department of Physics, University of California, Davis, California 95616, USA.

Senlei Li – Department of Physics, University of California, Davis, California 95616, USA.

Lang Wang – Department of Physics, University of California, Davis, California 95616, USA.

Notes

The authors declare no competing financial interest.

AUTHOR CONTRIBUTIONS

D. Y. and Y. H. designed the experiments. Y. H. synthesized Bi_2Se_3 nanoribbons and performed the measurements. R. X. and Y. H. performed numerical simulation. S. L. and L. W. assisted the synthesis and measurements. D. Y. and Y. H co-wrote the paper.

ACKNOWLEDGEMENTS

We thank Luke McClintock, H. Clark Travaglini, Antonio Rossi, Inna Vishik, Giacomo Resta, Sergey Savrasov, Rudro R. Biswas, and L. Andrew Wray for assistance in experiment and discussion. This work was supported by National Science Foundation Grant DMR-1838532 and DMR-1710737. This research used the Molecular Foundry, which is a US Department of Energy Office of Science User Facility under contract no. DE-AC02-05CH11231.

REFERENCES

(1) Kondou, K.; Yoshimi, R.; Tsukazaki, A.; Fukuma, Y.; Matsuno, J.; Takahashi, K. S.; Kawasaki, M.; Tokura, Y.; Otani, Y. Fermi-level-dependent charge-to-spin current conversion by Dirac surface states of topological insulators. *Nat. Phys.* **2016,** *12* (11), 1027-1031.

(2) Peng, X.; Yang, Y.; Singh, R. R. P.; Savrasov, S. Y.; Yu, D. Spin generation via bulk spin current in three-dimensional topological insulators. *Nat. Commun.* **2016,** *7* (1), 10878.

(3) Fu, L.; Kane, C. L. Superconducting Proximity Effect and Majorana Fermions at the Surface of a Topological Insulator. *Phys. Rev. Lett.* **2008,** *100* (9), 096407.

(4) Qu, D.-X.; Teslich, N. E.; Dai, Z.; Chapline, G. F.; Schenkel, T.; Durham, S. R.; Dubois, J. Onset of a Two-Dimensional Superconducting Phase in a Topological-Insulator--Normal-Metal $Bi_{1-x}Sb_x$/Pt Junction Fabricated by Ion-Beam Techniques. *Phys. Rev. Lett.* **2018,** *121* (3), 037001.

(5) Hou, Y.; Wang, R.; Xiao, R.; McClintock, L.; Clark Travaglini, H.; Paulus Francia, J.; Fetsch, H.; Erten, O.; Savrasov, S. Y.; Wang, B.; Rossi, A.; Vishik, I.; Rotenberg, E.; Yu, D. Millimetre-long transport of photogenerated carriers in topological insulators. *Nat. Commun.* **2019,** *10* (1), 5723.

(6) Pertsova, A.; Balatsky, A. V. Dynamically Induced Excitonic Instability in Pumped Dirac Materials. *Ann. Phys.* **2020,** *532* (2), 1900549.

(7) Kong, D.; Chen, Y.; Cha, J. J.; Zhang, Q.; Analytis, J. G.; Lai, K.; Liu, Z.; Hong, S. S.; Koski, K. J.; Mo, S.-K.; Hussain, Z.; Fisher, I. R.; Shen, Z.-X.; Cui, Y. Ambipolar field effect in the ternary topological insulator $(Bi_xSb_{1-x})_2Te_3$ by composition tuning. *Nat. Nanotechnol.* **2011,** *6* (11), 705-709.

(8) Hsieh, D.; Xia, Y.; Qian, D.; Wray, L.; Dil, J. H.; Meier, F.; Osterwalder, J.; Patthey, L.; Checkelsky, J. G.; Ong, N. P.; Fedorov, A. V.; Lin, H.; Bansil, A.; Grauer, D.; Hor, Y. S.; Cava, R. J.; Hasan, M. Z. A tunable topological insulator in the spin helical Dirac transport regime. *Nature* **2009,** *460* (7259), 1101-1105.

(9) King, P. D. C.; Hatch, R. C.; Bianchi, M.; Ovsyannikov, R.; Lupulescu, C.; Landolt, G.; Slomski, B.; Dil, J. H.; Guan, D.; Mi, J. L.; Rienks, E. D. L.; Fink, J.; Lindblad, A.; Svensson, S.; Bao, S.; Balakrishnan, G.; Iversen, B. B.; Osterwalder, J.; Eberhardt, W.; Baumberger, F.; Hofmann, P. Large Tunable Rashba Spin Splitting of a Two-Dimensional Electron Gas in Bi_2Se_3. *Phys. Rev. Lett.* **2011,** *107* (9), 096802.

(10) Rischau, C. W.; Leridon, B.; Fauqué, B.; Metayer, V.; van der Beek, C. J. Doping of Bi_2Te_3 using electron irradiation. *Phys. Rev. B* **2013,** *88* (20), 205207.

(11) Suh, J.; Yu, K. M.; Fu, D.; Liu, X.; Yang, F.; Fan, J.; Smith, D. J.; Zhang, Y.-H.; Furdyna, J. K.; Dames, C.; Walukiewicz, W.; Wu, J. Simultaneous Enhancement of Electrical Conductivity and Thermopower of Bi_2Te_3 by Multifunctionality of Native Defects. *Adv. Mater.* **2015,** *27* (24), 3681-3686.

(12) Zhu, Z. H.; Levy, G.; Ludbrook, B.; Veenstra, C. N.; Rosen, J. A.; Comin, R.; Wong, D.; Dosanjh, P.; Ubaldini, A.; Syers, P.; Butch, N. P.; Paglione, J.; Elfimov, I. S.; Damascelli, A. Rashba Spin-Splitting Control at the Surface of the Topological Insulator Bi_2Se_3. *Phys. Rev. Lett.* **2011,** *107* (18), 186405.

(13) Okada, Y.; Zhou, W.; Walkup, D.; Dhital, C.; Wilson, S. D.; Madhavan, V. Ripple-modulated electronic structure of a 3D topological insulator. *Nat. Commun.* **2012,** *3* (1), 1158.

(14) Kim, D.; Cho, S.; Butch, N. P.; Syers, P.; Kirshenbaum, K.; Adam, S.; Paglione, J.; Fuhrer, M. S. Surface conduction of topological Dirac electrons in bulk insulating Bi_2Se_3. *Nat. Phys.* **2012,** *8* (6), 459-463.

(15) Checkelsky, J. G.; Hor, Y. S.; Cava, R. J.; Ong, N. P. Bulk Band Gap and Surface State Conduction Observed in Voltage-Tuned Crystals of the Topological Insulator Bi_2Se_3. *Phys. Rev. Lett.* **2011,** *106* (19), 196801.

(16) Chen, J.; Qin, H. J.; Yang, F.; Liu, J.; Guan, T.; Qu, F. M.; Zhang, G. H.; Shi, J. R.; Xie, X. C.; Yang, C. L.; Wu, K. H.; Li, Y. Q.; Lu, L. Gate-Voltage Control of Chemical Potential and Weak Antilocalization in Bi_2Se_3.

Phys. Rev. Lett. **2010,** *105* (17), 176602.
(17) Kong, D.; Cha, J. J.; Lai, K.; Peng, H.; Analytis, J. G.; Meister, S.; Chen, Y.; Zhang, H.-J.; Fisher, I. R.; Shen, Z.-X.; Cui, Y. Rapid Surface Oxidation as a Source of Surface Degradation Factor for Bi_2Se_3. *ACS Nano* **2011,** *5* (6), 4698-4703.
(18) Benia, H. M.; Lin, C.; Kern, K.; Ast, C. R. Reactive Chemical Doping of the Bi_2Se_3 Topological Insulator. *Phys. Rev. Lett.* **2011,** *107* (17), 177602.
(19) Yeats, A. L.; Pan, Y.; Richardella, A.; Mintun, P. J.; Samarth, N.; Awschalom, D. D. Persistent optical gating of a topological insulator. *Sci. Adv.* **2015,** *1* (9), e1500640.
(20) Yeats, A. L.; Mintun, P. J.; Pan, Y.; Richardella, A.; Buckley, B. B.; Samarth, N.; Awschalom, D. D. Local optical control of ferromagnetism and chemical potential in a topological insulator. *Proc. Natl. Acad. Sci. U.S.A.* **2017,** *114* (39), 10379-10383.
(21) Sup Choi, M.; Lee, G.-H.; Yu, Y.-J.; Lee, D.-Y.; Hwan Lee, S.; Kim, P.; Hone, J.; Jong Yoo, W. Controlled charge trapping by molybdenum disulphide and graphene in ultrathin heterostructured memory devices. *Nat. Commun.* **2013,** *4* (1), 1624.
(22) Bertolazzi, S.; Krasnozhon, D.; Kis, A. Nonvolatile Memory Cells Based on MoS_2/Graphene Heterostructures. *ACS Nano* **2013,** *7* (4), 3246-3252.
(23) Wang, Q.; Wen, Y.; Cai, K.; Cheng, R.; Yin, L.; Zhang, Y.; Li, J.; Wang, Z.; Wang, F.; Wang, F.; Shifa, T. A.; Jiang, C.; Yang, H.; He, J. Nonvolatile infrared memory in MoS_2/PbS van der Waals heterostructures. *Sci. Adv.* **2018,** *4* (4), eaap7916.
(24) Yang, Y.; Peng, X.; Kim, H.-S.; Kim, T.; Jeon, S.; Kang, H. K.; Choi, W.; Song, J.; Doh, Y.-J.; Yu, D. Hot Carrier Trapping Induced Negative Photoconductance in InAs Nanowires toward Novel Nonvolatile Memory. *Nano Lett.* **2015,** *15* (9), 5875-5882.
(25) Yashina, L. V.; Sánchez-Barriga, J.; Scholz, M. R.; Volykhov, A. A.; Sirotina, A. P.; Neudachina, V. S.; Tamm, M. E.; Varykhalov, A.; Marchenko, D.; Springholz, G.; Bauer, G.; Knop-Gericke, A.; Rader, O. Negligible Surface Reactivity of Topological Insulators Bi_2Se_3 and Bi_2Te_3 towards Oxygen and Water. *ACS Nano* **2013,** *7* (6), 5181-5191.
(26) Ryu, S.; Mudry, C.; Obuse, H.; Furusaki, A. Z_2 Topological Term, the Global Anomaly, and the Two-Dimensional Symplectic Symmetry Class of Anderson Localization. *Phys. Rev. Lett.* **2007,** *99* (11), 116601.
(27) Fu, L.; Kane, C. L. Topology, Delocalization via Average Symmetry and the Symplectic Anderson Transition. *Phys. Rev. Lett.* **2012,** *109* (24), 246605.
(28) Ostrovsky, P. M.; Gornyi, I. V.; Mirlin, A. D. Interaction-Induced Criticality in Z_2 Topological Insulators. *Phys. Rev. Lett.* **2010,** *105* (3), 036803.
(29) Xu, Y.; Chiu, J.; Miao, L.; He, H.; Alpichshev, Z.; Kapitulnik, A.; Biswas, R. R.; Wray, L. A. Disorder enabled band structure engineering of a topological insulator surface. *Nat. Commun.* **2017,** *8* (1), 14081.
(30) Hong, S. S.; Cha, J. J.; Kong, D.; Cui, Y. Ultra-low carrier concentration and surface-dominant transport in antimony-doped Bi_2Se_3 topological insulator nanoribbons. *Nat. Commun.* **2012,** *3* (1), 757.
(31) Hou, Y.; Xiao, R.; Tong, X.; Dhuey, S.; Yu, D. In Situ Visualization of Fast Surface Ion Diffusion in Vanadium Dioxide Nanowires. *Nano Lett.* **2017,** *17* (12), 7702-7709.
(32) Kastl, C.; Guan, T.; He, X. Y.; Wu, K. H.; Li, Y. Q.; Holleitner, A. W. Local photocurrent generation in thin films of the topological insulator Bi_2Se_3. *Appl. Phys. Lett.* **2012,** *101* (25), 251110.
(33) Kastl, C.; Seifert, P.; He, X.; Wu, K.; Li, Y.; Holleitner, A. Chemical potential fluctuations in topological insulator $(Bi_{0.5}Sb_{0.5})_2Te_3$ -films visualized by photocurrent spectroscopy. *2D Mater.* **2015,** *2* (2), 024012.
(34) Kim, T.-H.; Baeck, J. H.; Choi, H.; Jeong, K.-H.; Cho, M.-H.; Kim, B. C.; Jeong, K. T. Phase

Transformation of Alternately Layered Bi/Se Structures to Well-Ordered Single Crystalline Bi_2Se_3 Structures by a Self-Organized Ordering Process. *J. Phys. Chem. C* **2012,** *116* (5), 3737-3746.
(35) Kim, Y. S.; Brahlek, M.; Bansal, N.; Edrey, E.; Kapilevich, G. A.; Iida, K.; Tanimura, M.; Horibe, Y.; Cheong, S.-W.; Oh, S. Thickness-dependent bulk properties and weak antilocalization effect in topological insulator Bi_2Se_3. *Phys. Rev. B* **2011,** *84* (7), 073109.
(36) Shewmon, P., *Diffusion in Solids*. Springer, Cham, Swizerland: 2016.
(37) Fanetti, M.; Mikulska, I.; Ferfolja, K.; Moras, P.; Sheverdyaeva, P. M.; Panighel, M.; Lodi-Rizzini, A.; Píš, I.; Nappini, S.; Valant, M.; Gardonio, S. Growth, morphology and stability of Au in contact with the Bi_2Se_3(0 0 0 1) surface. *Appl. Surf. Sci.* **2019,** *471*, 753-758.
(38) Shaughnessy, M. C.; Bartelt, N. C.; Zimmerman, J. A.; Sugar, J. D. Energetics and diffusion of gold in bismuth telluride-based thermoelectric compounds. *J. Appl. Phys.* **2014,** *115* (6), 063705.
(39) Kühne, M.; Paolucci, F.; Popovic, J.; Ostrovsky, P. M.; Maier, J.; Smet, J. H. Ultrafast lithium diffusion in bilayer graphene. *Nat. Nanotechnol.* **2017,** *12* (9), 895-900.
(40) Wang, R.; Erten, O.; Wang, B.; Xing, D. Y. Prediction of a topological p + ip excitonic insulator with parity anomaly. *Nat. Commun.* **2019,** *10* (1), 210.
(41) Miller, A.; Abrahams, E. Impurity Conduction at Low Concentrations. *Phys. Rev.* **1960,** *120* (3), 745-755.
(42) Kasap, S.; Capper, P., *Springer Handbook of Electronic and Photonic Materials*. 2nd ed.; Springer, Cham: Springer International Publishing AG, 2017.
(43) Shklovskii, B. I.; Levin, E. I.; Fritzsche, H.; Baranovskii, S. D., Hopping Photoconductivity in Amorphous Semiconductors: Dependence on Temperature, Electric Field and Frequency. In *Transport, Correlation, And Structural Defects*, World Scientific: Singapore: World Scientific: Singapore, 1990; pp 161-191.
(44) Rubel, O.; Baranovskii, S. D.; Thomas, P.; Yamasaki, S. Concentration dependence of the hopping mobility in disordered organic solids. *Phys. Rev. B* **2004,** *69* (1), 014206.
(45) Oelerich, J. O.; Nenashev, A. V.; Dvurechenskii, A. V.; Gebhard, F.; Baranovskii, S. D. Field dependence of hopping mobility: Lattice models against spatial disorder. *Phys. Rev. B* **2017,** *96* (19), 195208.
(46) Kaiser, W.; Albes, T.; Gagliardi, A. Charge carrier mobility of disordered organic semiconductors with correlated energetic and spatial disorder. *Phys. Chem. Chem. Phys.* **2018,** *20* (13), 8897-8908.
(47) Bianchi, M.; Guan, D.; Bao, S.; Mi, J.; Iversen, B. B.; King, P. D. C.; Hofmann, P. Coexistence of the topological state and a two-dimensional electron gas on the surface of Bi_2Se_3. *Nat. Commun.* **2010,** *1* (1), 128.
(48) Dai, J.; West, D.; Wang, X.; Wang, Y.; Kwok, D.; Cheong, S. W.; Zhang, S. B.; Wu, W. Toward the Intrinsic Limit of the Topological Insulator Bi_2Se_3. *Phys. Rev. Lett.* **2016,** *117* (10), 106401.
(49) Alpichshev, Z.; Biswas, R. R.; Balatsky, A. V.; Analytis, J. G.; Chu, J. H.; Fisher, I. R.; Kapitulnik, A. STM Imaging of Impurity Resonances on Bi_2Se_3. *Phys. Rev. Lett.* **2012,** *108* (20), 206402.
(50) Zhang, C.; Yuan, X.; Wang, K.; Chen, Z.-G.; Cao, B.; Wang, W.; Liu, Y.; Zou, J.; Xiu, F. Observations of a Metal–Insulator Transition and Strong Surface States in $Bi_{2-x}Sb_xSe_3$ Thin Films. *Adv. Mater.* **2014,** *26* (41), 7110-7115.

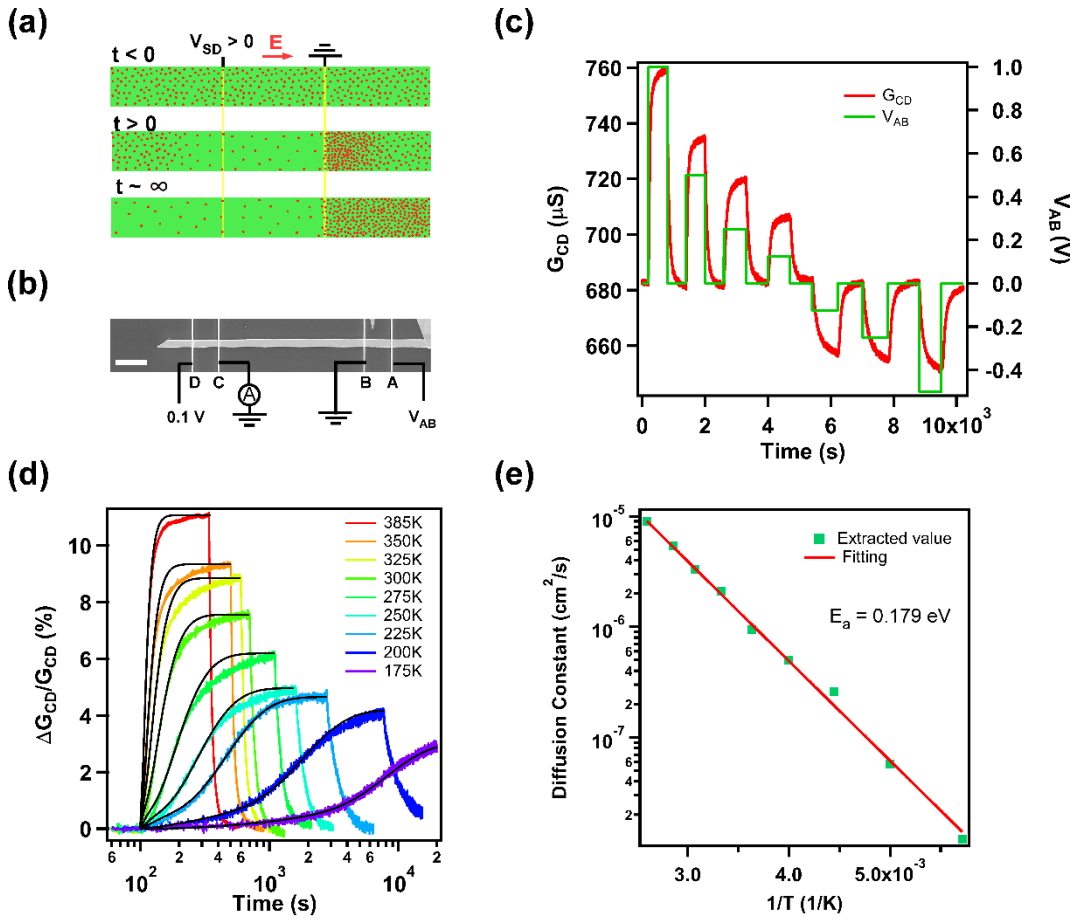

Figure 1. Temperature dependent electric-field-driven non-local conductance tuning**.** (a) Schematic of trapped charge migration with electric field applied after t = 0 s in the middle section of the device. Red dots represent charges trapped at the defect states. (b) SEM image of a TI nanoribbon device (device #1) with four top metal contacts. Scale bar denotes 50 μm. (c) G_{CD} and V_{AB} as a function of time at 300 K. G_{CD} was monitored by a small bias on channel CD. (d) Time trace of percentage change in G_{CD} in response to V_{AB} at various temperatures. V_{AB} = 0.5 V was turned on at 100 s for all temperatures and off when G_{CD} reached saturation. Black curves are simulated responses using a diffusion model. (e) Semi-log plot of diffusion constant extracted from d as a function of inverse temperature. The red curve is fitting by an Arrhenius equation with an activation energy E_a = 0.179 eV.

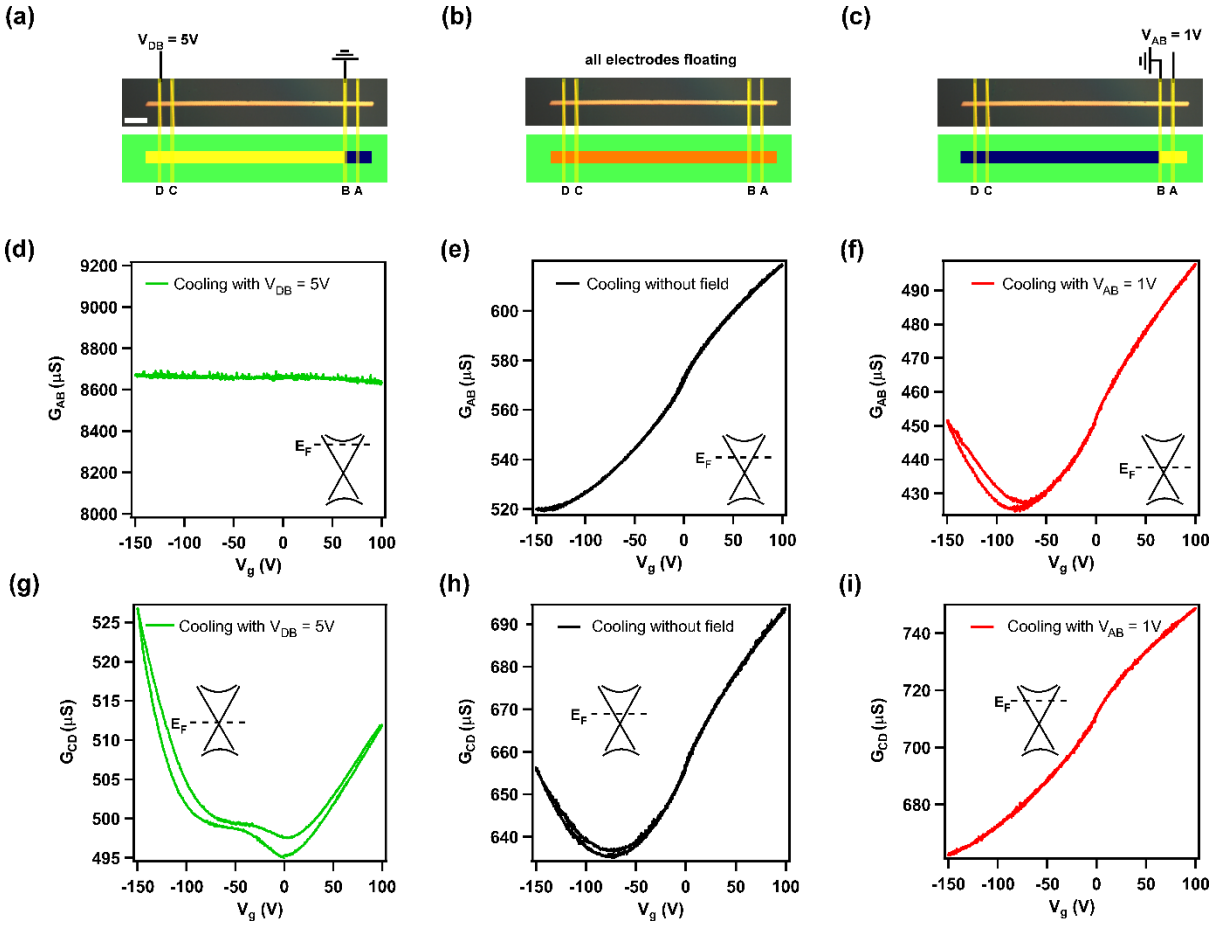

Figure 2. Field cooling effects on conductance and gate response. (a-c) Optical image of device #2 and schematics showing three biasing conditions. Scale bar denotes 50 μm. The color codes indicate the conductivity change after cooling to 77 K: orange, no change; yellow, less *n*-type; dark blue, more *n*-type. (d-i) Gate responses of channels AB (d-f) and CD (g-i) at 77 K, respectively, after cooling under different biasing conditions. Insets: energy diagrams showing E_F modulation in the channel.

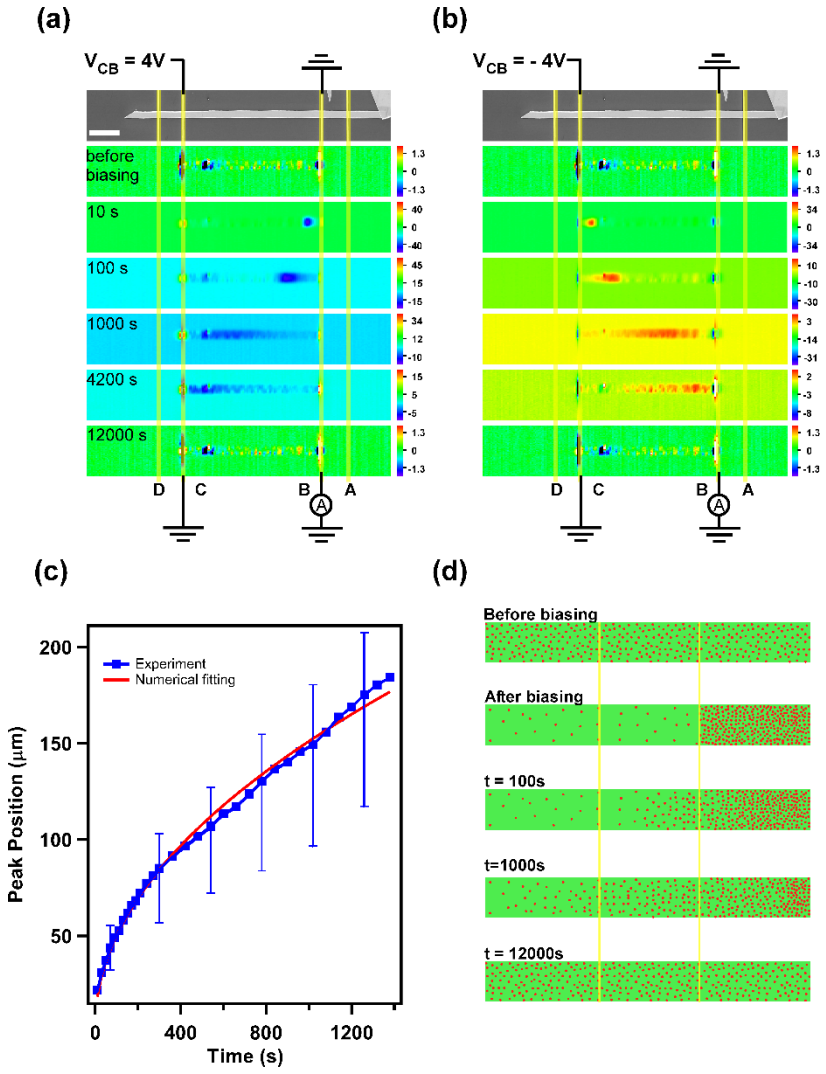

Figure 3. Visualization of field-induced doping gradient in a TI nanoribbon by photocurrent mapping. All photocurrent images were taken at 200 K and zero-bias for device #1. (a) Optical image and photocurrent images taken at different times. The first photocurrent image was taken after the device was cooled to 200 K in the absence of electric field. Then V_{CB} = 4 V was held for 3 hrs. The rest photocurrent images were taken at the indicated times after V_{CB} was reduced to 0 V at t = 0 s. The laser wavelength was 532 nm and its power was 50 μW. Color scales are in nA. Scale bar denotes 50 μm. (b) Similar measurements performed for V_{CB} = - 4 V. (c) Photocurrent peak position in A as a function of time. The position of contact B is taken as origin. The red curve is square root fitting. The "error bars" at representative data points indicate the full width at half maximum (FWHM) of the photocurrent peaks. (d) Schematic drawings of the distribution of trapped holes at each stage.

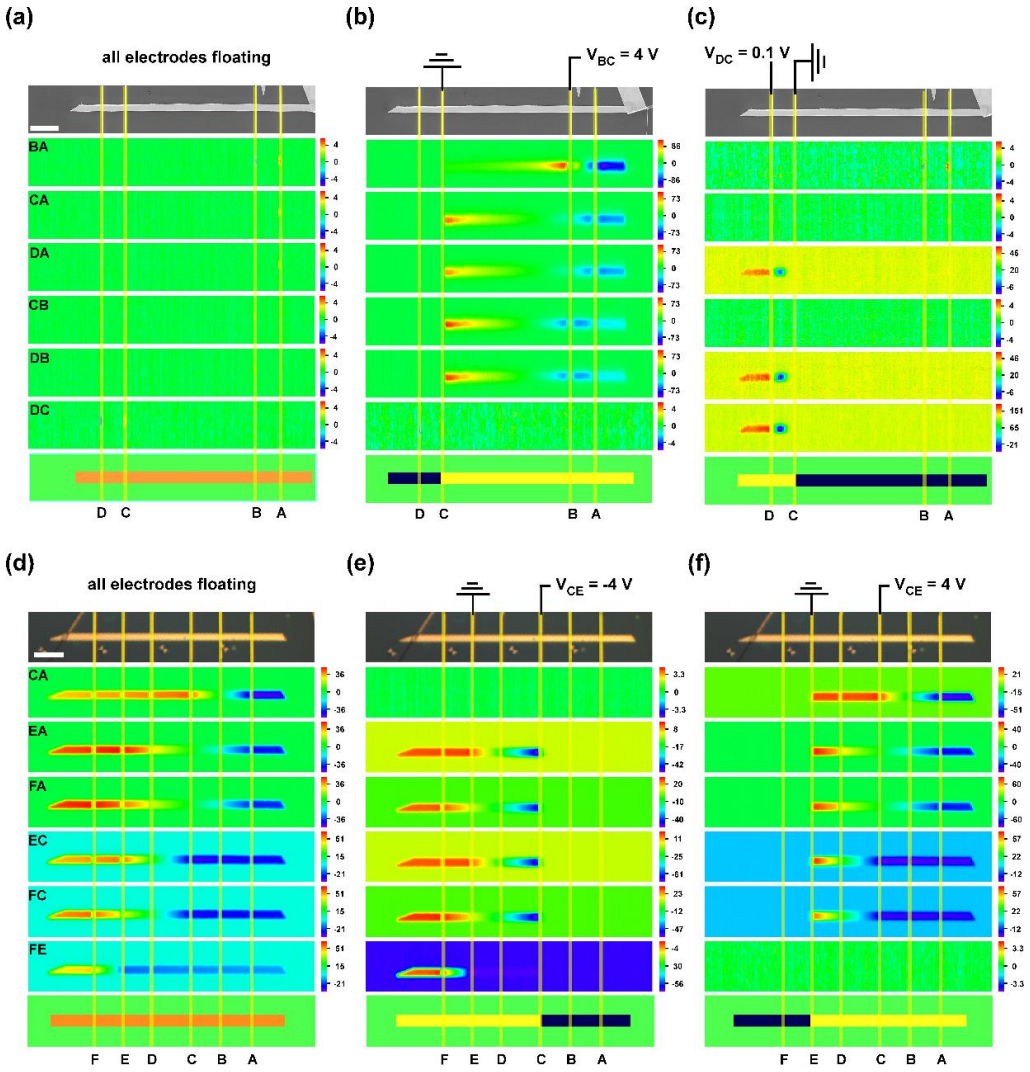

Figure 4. Field effects on photocurrent decay length. Devices were cooled from room temperature to 77 K under different biasing conditions as specified on the optical images at the top. All photocurrent images were taken at 77 K and zero-bias. (a-c) Device #1. Scale bar denotes 50 μm and laser power is 2.3 μW. (d-f) Device #3. Scale bar denotes 30 μm and laser power is 0.50 μW. Photocurrent images were taken with different connections as indicated in each row. For example, BA means that contact B is directly grounded and A is connected to ground through a preamplifier. The bottom row is a schematic drawing indicating the field-induced conductivity change: orange, no change; yellow, less *n*-type; dark blue, more *n*-type. Color scales are in nA.

TOC FIGURE